



Theoretical Limits on Cooperative Positioning in Mixed Traffic

Downloaded from: <https://research.chalmers.se>, 2026-04-07 00:04 UTC

Citation for the original published paper (version of record):

Steinmetz, E., Emardson, R., Brännström, F. et al (2019). Theoretical Limits on Cooperative Positioning in Mixed Traffic. IEEE Access, 7: 49712-49725.

<http://dx.doi.org/10.1109/ACCESS.2019.2910658>

N.B. When citing this work, cite the original published paper.

© 2019 IEEE. Personal use of this material is permitted. Permission from IEEE must be obtained for all other uses, in any current or future media, including reprinting/republishing this material for advertising or promotional purposes, or reuse of any copyrighted component of this work in other works.

Theoretical Limits on Cooperative Positioning in Mixed Traffic

Erik Steinmetz, Ragne Emardson, Fredrik Brännström, and Henk Wymeersch

Abstract—A promising solution to meet the demands on accurate positioning and real time situational awareness in future intelligent transportation systems (ITS) is cooperative positioning, where vehicles share sensor information over the wireless channel. However, the sensing and communication technologies required for this will be gradually introduced into the market, and it is therefore important to understand what performance we can expect from cooperative positioning systems as we transition to a more modern vehicle fleet. In this paper, we study what effects a gradual market penetration has on cooperative positioning applications, through a Fisher information analysis. Simulation results indicate that solely introducing a small fraction of automated vehicles with high-end sensors significantly improves the positioning quality, but is not enough to meet the stringent demands posed by safety critical ITS applications. Furthermore, we find that retrofitting vehicles with low-cost satellite navigation receivers and communication have marginal impact when the positioning requirements are stringent, and that longitudinal road position can be estimated more accurately than lateral.

I. INTRODUCTION

IN future intelligent transportation systems (ITS), vehicles are envisioned to be automated and safely navigate our streets [1]. A key factor for this to become a reality is accurate self-positioning and real-time situational awareness. To this end, vehicles will be equipped with the latest sensors (such as global navigation satellite systems (GNSS) receivers, radars, lidars, stereo-cameras etc.) for positioning of both the ego vehicle with respect to a high-definition (HD) map, and sensing of other objects in the dynamically changing environment [2], [3]. On top of this, vehicles are expected to be connected to each other and the cloud [4]–[6]. This allows for cooperation between vehicles, both when it comes to coordination and control as in [7], [8] and for cooperative positioning and mapping of the environment [9]–[14] to improve position accuracy and extend the situational awareness beyond the field of view (FOV) of traditional on-board sensors. In particular, wireless communication makes it possible to build a local dynamic map (LDM), either in each vehicle

or centrally in the cloud, containing both static HD map information as well as information about where other dynamic objects such as vehicles and pedestrians are positioned. This information can then be used to increase the situational awareness for human drivers, or as input to automated driving systems. However, the requirements on the map might vary depending on the underlying use case/application. Typical positioning requirements range from tens of centimeters (e.g., for cooperative automated driving) to meter level accuracies for less safety-critical applications [15]–[17]. Commonly the requirement specified for a particular use case/application is fixed independent of the relative location between vehicles, though there might be different accuracy requirements for the longitudinal and lateral road position [3].

Market penetration of the technologies required for this type of cooperative applications will however be gradual. According to [18] about 50% of the vehicles in the European fleet of passenger cars are over ten years old, and approximately 5% of new vehicles are introduced each year. Out of these, only a small fraction will be automated, and global market uptake projections [19], [20] forecast that it will take until 2035 before 25% of the new vehicles that reach the market are either automated or partially automated. On the other hand, many of the main automotive original equipment manufacturers (OEMs), such as Volkswagen Group, Toyota, General Motors, and Daimler Trucks have already announced that they are rolling out connected cars within the near future [21], and we will most likely see a faster market penetration when it comes to connectivity [22]. Nonetheless, this means that for a transition period the vehicles on our road will have greatly varying sensing and communication capabilities, ranging from state-of-the-art sensing and communication to no sensing and communication capabilities at all. From a system perspective, it is therefore important to understand how the penetration rate of modern vehicles with extensive sensing capabilities affects the possibility to build up a shared LDM, and under which circumstances it is possible to meet the accuracy requirements posed by different ITS applications.

The aim of this paper is to study the effect a gradual market penetration will have on cooperative positioning. In particular, we will focus on the application of building up an LDM in which both the ego vehicle and other cooperative and non-cooperative vehicles are positioned, and investigate how the penetration rate of vehicles with extensive sensing capabilities affects the possibility to build such a map.

E. Steinmetz, F. Brännström and H. Wymeersch are with the Communication Systems Group, Department of Electrical Engineering, Chalmers University of Technology, Gothenburg, Sweden, e-mails: erik.steinmetz@ri.se, {fredrik.brannstrom, henkw}@chalmers.se. E. Steinmetz is also with the Division of Safety and Transport at RISE Research Institutes of Sweden, Borås, Sweden. R. Emardson is with University of Borås, Borås, Sweden (e-mail: ragne.emardson@hb.se). This research was supported, in part, by the National Metrology Institute hosted at RISE Research Institutes of Sweden, which in turn is partly funded by VINNOVA under the program for national metrology (grant 2015-06478); the PRoPART (Precise and Robust Positioning for Automated Road Transport) project, funded by the European GNSS Agency under the EU H2020 program (grant 776307).

A. Related Work

Though none or very few commercial applications of cooperative positioning exist yet, the topic has been extensively researched [9]–[14], [23]–[32]. We can group existing works into two categories depending on if *communication-based* or *noncommunication-based* sensing techniques are used to generate the measurements between agents (in our case vehicles).

Communication-based sensing includes various types of radio communication technologies, such as ultra-wide bandwidth (UWB), 4G LTE, 802.11p, and 5G communication. Cooperative positioning with UWB ranging has been considered in [23], [24], while [25], [26] considers 802.11p-based range and range rate measurements. So far, communication-based sensing has gained very little traction in the automotive sector, mainly because of the relatively poor accuracy in the measurements from 802.11p and 4G LTE based ranging, and the requirement of additional infrastructure as in the case of UWB. Note that with the introduction of 5G this might change, as 5G is expected to provide both high speed connectivity as well as accurate ranging and new types of measurements such as angle of arrival (AoD) and angle of departure (AoD) measurements [27].

Noncommunication-based sensing includes technologies that perceive objects in the environment, but don't explicitly communicate with these objects. Examples are radars, lidars, stereo-cameras, HD-video, ultrasonic sensors. As many of these sensors already are extensively used within the automotive industry it is natural to utilize this information in cooperative positioning algorithms. In addition, this type of sensors can also provide information about non-cooperative agents or objects. Cooperative positioning where vehicles share data from noncommunication-based sensors has been considered in [10]–[14]. Out of these, [10]–[12] consider radar-based sensor fusion, while [13] uses a camera-based solution for plausibility of cooperative awareness messages (CAMs), and [14] considers a combination of camera and lidar information. Another interesting aspect of this problem is whether or not the information received over the wireless channel is used to improve the position estimate of the own vehicle [9], or if the primary purpose is to provide a lifted-seat or see-through functionality [14].

For both communication-based and noncommunication-based sensing, fundamental insights can be gleaned from theoretical performance limits. The literature is rich when it comes to performance limits for cooperative positioning systems in the communication-based sensing category [28]–[31] and only a few, e.g., [30], [31] specifically targets the vehicular setting. Thus, there is a need to better quantify the performance of cooperative position in vehicular networks with noncommunication-based sensors. Furthermore, to the best of our knowledge no previous works have analyzed how the composition of the vehicle fleet and the gradual penetration of vehicles with high-end sensors impacts the positioning quality, and the possibility to meet accuracy requirements posed by different ITS applications. However, a recent work [32] highlights that it is important to gain an understanding of how penetration rates impacts performance, and presents a

stochastic geometry model for evaluation of sensor coverage and redundancy in a collaborative sensing scenario.

B. Contributions

In this paper, we aim to understand how the sensing capability in a given vehicle fleet affects the possibility to build a shared LDM. We provide a detailed description of how to construct the Fisher information matrix (FIM) for an arbitrary sized and configured vehicle fleet. Based on the FIM we compute what is called the position error bound (PEB), which provides a lower bound on the theoretically achievable estimation accuracy for each vehicle's position. Moreover, we apply the notion of equivalent Fisher information (EFI) to provide a geometric interpretation of how different types of observations (such as GNSS, compass and radar) contribute to reducing the positioning uncertainty. Our main contributions are:

- A framework and method based on Fisher information analysis and Cramér-Rao bounds to determine the fundamental limits for cooperative positioning in a scenario, where vehicles share information from on-board GNSS, compass, and radar sensors to build up a joint LDM in an attempt to increase the knowledge of both their own and other's position.
- A novel analysis where we show how the composition of the vehicle fleet, and thus the penetration rate of vehicles with extensive sensing capability, affects the possibility to build an LDM that meets the positioning requirements posed by different ITS applications.

While the analysis in the paper is generally applicable, we focus on a multi-lane freeway scenario, with four types of vehicles ranging from legacy vehicles with neither sensing nor communication capability to automated vehicles with high-end sensors and communication capability. Also, note that the bounds presented in this paper give an indication of what measurement uncertainties can be expected from future cooperative vehicular positioning systems.

C. Notation

In this paper, matrices are denoted by uppercase bold letters, e.g., \mathbf{X} , (column) vectors are denoted by lowercase bold letters, e.g., \mathbf{x} . Vectors can be stacked as $\mathbf{x} = [\mathbf{x}_1; \mathbf{x}_2; \mathbf{x}_3]$, and the stack of vectors $[\mathbf{x}_1; \dots; \mathbf{x}_N]$ is denoted $[\mathbf{x}_i]_{i \in \{1 \dots N\}}$. The transpose of a matrix \mathbf{X} is denoted by \mathbf{X}^T , $[\mathbf{X}]_{i,j}$ represents block (i, j) of a matrix, where the size depends on the context. \mathbf{I}_k is the $k \times k$ identity matrix and $\mathbf{0}_{k,l}$ is the $k \times l$ zero matrix. Furthermore, $1_{\{x \in \mathcal{X}\}}$ denotes the indicator function which is one if $x \in \mathcal{X}$ and zero otherwise. Finally, $\nabla_{\mathbf{x}}$ denotes the gradient of \mathbf{x} .

II. SYSTEM MODEL

In this section, we describe the scenario and the sensor models consider in this paper, and formulate the problem that we will focus on.

A. Scenario

We consider a heterogeneous traffic scenario with a set $\mathcal{V} = \{1 \dots N\}$ of N vehicles with varying sensing and communication capabilities, as well as a central fusion server (e.g., a road side unit or dedicated vehicle). We model vehicles as point objects and denote the unknown state of vehicle $i \in \mathcal{V}$ as \mathbf{x}_i , comprising the absolute position $\mathbf{p}_i \in \mathbb{R}^2$ in a global frame of reference, the heading $\psi_i \in \mathbb{R}$ and the type T_i , where the latter relates to sensing and communication abilities of the vehicle. In reality, vehicles can be equipped with a multitude of sensors and communication technologies. For simplicity, we focus on four distinct types $T_i \in \{A, M, R, L\}$:

- A: **Automated vehicles:** Equipped with 360° radar, compass, high-accuracy GNSS module, and a communication radio.
- M: **Modern vehicles:** Equipped with forward looking radar, compass, low-cost GNSS module, and a communication radio.
- R: **Retrofitted vehicles:** Equipped with low-cost GNSS module and a communication radio.
- L: **Legacy vehicles:** Neither sensing nor communication capabilities.

and let $\boldsymbol{\rho} = [\rho_A \ \rho_M \ \rho_R \ \rho_L]$ represent the fraction of automated, modern, retrofitted and legacy vehicles in the system.¹ Moreover, we denote the set of automated, modern, retrofitted, and legacy vehicles by \mathcal{V}_A , \mathcal{V}_M , \mathcal{V}_R and \mathcal{V}_L , respectively. The set of adjacent vehicles, i.e., vehicles that can be observed by a vehicle i using its radar, is denoted \mathcal{A}_i . Note that for legacy and retrofitted vehicles $\mathcal{A}_i = \emptyset$. For notational convenience, we also denote the set of vehicles that have a GNSS module on board as $\mathcal{V}_G = \mathcal{V}_A \cup \mathcal{V}_M \cup \mathcal{V}_R$.

B. Sensor Models

While our analysis holds for any observation model, the three types of observations we will consider are the following:

- 1) **GNSS:** Observations made by vehicle $i \in \mathcal{V}_G$ of its own position using the GNSS module are modeled as [12]

$$\mathbf{y}_{ii}^G = \mathbf{f}_{ii}^G(\mathbf{x}_i, \mathbf{x}_i) + \mathbf{n}_{ii}^G = \mathbf{p}_i + \mathbf{n}_{ii}^G, \quad (1)$$

where $\mathbf{n}_{ii}^G \sim \mathcal{N}(0, \boldsymbol{\Sigma}_{ii})$ and $\boldsymbol{\Sigma}_{ii} = \sigma_{G,i}^2 \mathbf{I}_2$.

- 2) **Compass:** Observations made by vehicle $i \in \mathcal{V}_A \cup \mathcal{V}_M$ of its own heading using the compass sensor are modeled as [12]

$$y_{ii}^C = f_{ii}^C(\mathbf{x}_i, \mathbf{x}_i) + n_{ii}^C = \psi_i + n_{ii}^C \quad (2)$$

where $n_{ii}^C \sim \mathcal{N}(0, \sigma_{C,i}^2)$.

- 3) **Radar:** The sensor FOV is determined by an opening angle θ_{FOV} and a maximum detection range r_{max} . Observations are, similar to [11], [12], modeled as relative positions in the ego vehicle coordinate frame, i.e.,

$$\mathbf{y}_{ij}^R = \mathbf{f}_{ij}^R(\mathbf{x}_i, \mathbf{x}_j) + \mathbf{n}_{ij}^R = \mathbf{R}(\psi_i)(\mathbf{p}_j - \mathbf{p}_i) + \mathbf{n}_{ij}^R, \quad (3)$$

where $\mathbf{n}_{ij}^R \sim \mathcal{N}(0, \boldsymbol{\Sigma}_{ij})$ and

$$\mathbf{R}(\psi_i) = \begin{bmatrix} \cos(\psi_i) & \sin(\psi_i) \\ -\sin(\psi_i) & \cos(\psi_i) \end{bmatrix} \quad (4)$$

is the rotation matrix between the global coordinate frame and the ego vehicle coordinate frame. Since radars typically make mutually independent measurements in range (r) and bearing (α) the noise components when transformed from a polar to a cartesian coordinate frame are not mutually independent. We approximate the covariance of the radar measurements in the cartesian ego vehicle frame as

$$\boldsymbol{\Sigma}_{ij} = \mathbf{R}^T(\alpha_{ij}) \boldsymbol{\Sigma}_{ij}^{P*} \mathbf{R}(\alpha_{ij}) \quad (5)$$

where $\boldsymbol{\Sigma}_{ij}^{P*} = \text{diag}([\sigma_{r,i}^2, (r_{ij}\sigma_{\alpha,i})^2])$ is an approximation of the covariance in a cartesian coordinate system $\{P^*\}$ aligned with the radial and angular axis of the original polar coordinate system. Furthermore, $\sigma_{r,i}$ and $\sigma_{\alpha,i}$ are the standard deviations of the mutually independent noise components of the range and bearing measurements in the original polar coordinate system, and r_{ij} and α_{ij} are the range and bearing between vehicle i and j , respectively.

C. Problem Statement

We define the LDM as the estimated locations of all (or a subset) of the vehicles at the fusion center. To gain insights on how the penetration rates of the different vehicle types $\boldsymbol{\rho} = [\rho_A \ \rho_M \ \rho_R \ \rho_L]$ affects the quality of the LDM, we will derive lower bounds on the position accuracies as a function of those penetration rates and assess under which conditions a target accuracy denoted P_t can be attained.

Limitations: The analysis and bounds derived in this paper are valid for point targets, and assumes perfect data association, i.e., that each measurement is perfectly associated to a target. Also, we do not implement any model for sensor blockage, i.e., that vehicles might be occluded behind other vehicles. Furthermore, the bounds presented here are snapshot bounds, i.e., they do not take into account prior information, but are based on the measurements available at a certain time instance. Posterior CRLBs could be considered, but has the drawback that they require assumptions about specific vehicle trajectories and dynamic models [31]. Note that ideal data association and not accounting for blocking effects might lead to overly optimistic bounds, while not accounting for prior information might lead to overly conservative bounds if comparing to a tracking algorithm. In regards to the assumption of point targets, modeling of extended targets [33] require more advanced sensor models with a more complex relation to the individual vehicle positions. Finally, the simulation results are limited to fixed target accuracies P_t , that do not depend on the relative distance between vehicles.

III. PRELIMINARIES

A. FIM and CRLB

The Cramér-Rao lower bound (CRLB) expresses a bound on the variance of unbiased estimators for deterministic but unknown parameters and can be used to obtain insights about the

¹Note that the even though the fourth type is called legacy vehicle it could be used to include also other non-cooperative agents such as pedestrians.

quality of estimation algorithms. The CRLB on the covariance of an unbiased estimator $\hat{\boldsymbol{\theta}}$ of a parameter $\boldsymbol{\theta} = [\boldsymbol{\theta}_1; \dots; \boldsymbol{\theta}_K]$ can be expressed as

$$\mathbf{J}^{-1}(\boldsymbol{\theta}) \preceq \mathbb{E} \left\{ (\boldsymbol{\theta} - \hat{\boldsymbol{\theta}})(\boldsymbol{\theta} - \hat{\boldsymbol{\theta}})^T \right\}, \quad (6)$$

where $\mathbf{J}(\boldsymbol{\theta}) = -\mathbb{E}_{\mathbf{y}} \left\{ \nabla_{\boldsymbol{\theta}}^T \nabla_{\boldsymbol{\theta}} \log p(\mathbf{y}|\boldsymbol{\theta}) \right\}$ is the Fisher information matrix (FIM), derived from the likelihood $p(\mathbf{y}|\boldsymbol{\theta})$. For the case of Gaussian observations $\mathbf{y} \sim \mathcal{N}(\mathbf{f}(\boldsymbol{\theta}), \boldsymbol{\Sigma})$, the FIM is given by

$$\mathbf{J}(\boldsymbol{\theta}) = \nabla_{\boldsymbol{\theta}}^T \mathbf{f}(\boldsymbol{\theta}) \boldsymbol{\Sigma}^{-1} \nabla_{\boldsymbol{\theta}} \mathbf{f}(\boldsymbol{\theta}). \quad (7)$$

B. EFIM

The equivalent Fisher information matrix (EFIM) is a tool to extract the information required to compute the CRLB for a subset of the parameter vector $\boldsymbol{\theta}$. More precisely, given a parameter vector $\boldsymbol{\theta} = [\boldsymbol{\theta}_1; \boldsymbol{\theta}_2]$ with corresponding FIM

$$\mathbf{J}(\boldsymbol{\theta}) = \begin{bmatrix} \mathbf{A} & \mathbf{B} \\ \mathbf{B}^T & \mathbf{C} \end{bmatrix} \quad (8)$$

where $\boldsymbol{\theta}_1 \in \mathbb{R}^m$, $\boldsymbol{\theta}_2 \in \mathbb{R}^n$, $\mathbf{A} \in \mathbb{R}^{m \times m}$, $\mathbf{B} \in \mathbb{R}^{m \times n}$ and $\mathbf{C} \in \mathbb{R}^{n \times n}$ the EFIM is defined as [28]

$$\mathbf{J}_e(\boldsymbol{\theta}_1) = \mathbf{A} - \mathbf{B}\mathbf{C}^{-1}\mathbf{B}^T. \quad (9)$$

Note that the EFIM retains all the information regarding the parameter vector $\boldsymbol{\theta}_1$ in the sense that $\mathbf{J}_e^{-1}(\boldsymbol{\theta}_1) = [\mathbf{J}^{-1}(\boldsymbol{\theta})]_{1,1}$, in which $[\cdot]_{1,1}$ extracts the $m \times m$ block pertaining to $\boldsymbol{\theta}_1$.

C. PEB

Given the collection of measurements \mathbf{y} available at the fusion center and the associated FIM, the position error bound (PEB) of vehicle i is defined as

$$\mathcal{P}(\mathbf{p}_i) = \begin{cases} \sqrt{\text{tr} \{ \mathbf{J}_e^{-1}(\mathbf{p}_i) \}} & i \in \mathcal{J}_P \\ +\infty & i \notin \mathcal{J}_P \end{cases} \quad (10)$$

where \mathcal{J}_P is the set of vehicles for which the position is identifiable (see Section IV-B) in a Fisher information sense.

IV. ANALYSIS OF THE FIM

A. General Expression

We write the vector of unknown parameters as

$$\boldsymbol{\theta} = [\mathbf{p}; \boldsymbol{\psi}], \quad (11)$$

where \mathbf{p} is the vector of positions $\mathbf{p} = [\mathbf{p}_1; \mathbf{p}_2; \dots; \mathbf{p}_N]$ and $\boldsymbol{\psi}$ is the vector of vehicle headings $\boldsymbol{\psi} = [\psi_1; \dots; \psi_N]$. The measurements available to estimate these parameters depends on the network topology, which in turn depends on the specific vehicle types and on who can observe who. We can express the vector of measurements available to the central fusion server as

$$\mathbf{y} = \left[\begin{array}{c} [\mathbf{y}_{ii}^G]_{i \in \mathcal{V}_G}; \\ [\mathbf{y}_{ii}^C]_{i \in \mathcal{V}_A \cup \mathcal{V}_M}; \\ [\mathbf{y}_{ij}^R]_{i \in \mathcal{V}_A \cup \mathcal{V}_M, j \in \mathcal{A}_i} \end{array} \right]. \quad (12)$$

Note that radar measurements between a vehicle i and j only are included if $j \in \mathcal{A}_i$. Based on this, we can then write the

joint likelihood of all the measurements available to the central fusion server as

$$p(\mathbf{y}|\boldsymbol{\theta}) = \mathcal{N}(\mathbf{f}(\boldsymbol{\theta}), \boldsymbol{\Sigma}) \quad (13)$$

where $\mathbf{f}(\boldsymbol{\theta})$ is a vector of the mean functions and $\boldsymbol{\Sigma}$ is a block diagonal matrix with the measurement uncertainties corresponding to each measurement. Based on this we then find that the FIM $\mathbf{J}(\boldsymbol{\theta})$, given by (7), is $3N \times 3N$ matrix structured as in Proposition 1.

Proposition 1. *Given the scenario and sensor models outlined in Section II we can express the FIM as*

$$\mathbf{J}(\boldsymbol{\theta}) = \begin{bmatrix} \mathbf{A} & \mathbf{B} \\ \mathbf{B}^T & \mathbf{C} \end{bmatrix} \quad (14)$$

where \mathbf{A} is a $2N \times 2N$ matrix, consisting of 2×2 blocks, where block (i, j)

$$[\mathbf{A}]_{i,j} = \begin{cases} 1_{\{i \in \mathcal{V}_G\}} \boldsymbol{\Sigma}_{ii}^{-1} + \sum_{j' \in \mathcal{A}_i} \mathbf{S}_{ij'} + \sum_{j' : i \in \mathcal{A}_{j'}} \mathbf{S}_{j'i} & i = j \\ -1_{\{j \in \mathcal{A}_i\}} \mathbf{S}_{ij} - 1_{\{i \in \mathcal{A}_j\}} \mathbf{S}_{ji} & i \neq j \end{cases} \quad (15)$$

\mathbf{B} is a $2N \times N$ matrix, consisting of 2×1 blocks, where block (i, j)

$$[\mathbf{B}]_{i,j} = \begin{cases} -\sum_{j' \in \mathcal{A}_i} \frac{1}{r_{ij'} \sigma_{\alpha,i}^2} \mathbf{R}^T \left(\frac{\pi}{2} \right) \mathbf{u}_{ij'} & i = j \\ 1_{\{i \in \mathcal{A}_j\}} \frac{1}{r_{ji} \sigma_{\alpha,j}^2} \mathbf{R}^T \left(\frac{\pi}{2} \right) \mathbf{u}_{ji} & i \neq j \end{cases} \quad (16)$$

and \mathbf{C} is a $N \times N$ diagonal matrix with elements (i, j) of the form

$$[\mathbf{C}]_{i,j} = \begin{cases} 1_{\{i \in \mathcal{V}_A \cup \mathcal{V}_M\}} \frac{1}{\sigma_{\alpha,i}^2} + \sum_{j \in \mathcal{A}_i} \frac{1}{\sigma_{\alpha,i}^2}, & i = j \\ 0 & i \neq j \end{cases} \quad (17)$$

in which $\mathbf{S}_{ij} = \mathbf{R}^T(\psi_i) \boldsymbol{\Sigma}_{ij}^{-1} \mathbf{R}(\psi_i)$, and $\mathbf{u}_{ij} = [\cos(\beta_{ij}) \quad \sin(\beta_{ij})]^T$ is the unit vector pointing in the direction $\beta_{ij} = \psi_i + \alpha_{ij}$.

Proof: See Appendix A. ■

The matrix \mathbf{A} in Proposition 1 correspond to the Fisher information that the observations carry about the positions \mathbf{p} when the headings $\boldsymbol{\psi}$ are known. The diagonal blocks of \mathbf{A} consist of three positive definite terms: the information from the GNSS observation, the information from radar observations that vehicle i makes of other vehicles $j \in \mathcal{A}_i$, and the information from radar observations by other vehicles that observe vehicle i . The first term is directly the inverse of the GNSS observation covariance $\boldsymbol{\Sigma}_{ii}$, while \mathbf{S}_{ij} in the radar terms can be interpreted as the inverse of the radar observation covariance $\boldsymbol{\Sigma}_{ij}$ represented in the global coordinate frame. The off-diagonal blocks (i, j) , $i \neq j$ are negative definite and correspond to the reduction of information of the radar observations due to the measuring or measured vehicle's unknown position (note that in the absence of GNSS observations, the matrix \mathbf{A} is singular, so that the positions would not be identifiable). The matrix \mathbf{C} is a diagonal matrix with diagonal entries comprising the information from the compass and from the radar signals that vehicle takes with respect to its neighbors. The off-diagonal elements are zero

since the heading of a vehicle observed by a radar does not affect the radar measurement, i.e., when vehicle i observes vehicle j with the radar the measurement \mathbf{y}_{ij} does not depend on ψ_j . Finally, \mathbf{B} describes the information coupling between positions and headings, which occurs due to the fact that the information about the positions from a radar observation depends on the unknown heading of the observing vehicle, and similarly that the information radars bring about the heading of the observing vehicle depend on the unknown positions of both observing and observed vehicle.

B. Identifiable Vehicles

The measurement vector \mathbf{y} might not contain sufficient information to identify all the unknown parameters in $\boldsymbol{\theta}$, leading to non-invertible FIM. By removing unidentifiable vehicles, the FIM can be rendered full-rank. To this end we introduce the two sets \mathcal{J}_P and \mathcal{J}_H , which are sets containing the indices of the identifiable positions and headings, respectively. The procedure for generating the sets is highly dependent on the specific scenario and sensing models. In Algorithm 1 we illustrate how to compute the sets \mathcal{J}_P and \mathcal{J}_H for the specific scenario and sensing models outlined in Section II.

Algorithm 1 Computation of \mathcal{J}_P and \mathcal{J}_H

- 1: $\mathcal{J}_P = \emptyset, \mathcal{J}_H = \emptyset$
 - 2: **for** $i = 1 : N$ **do**
 - 3: if $i \in \mathcal{V}_A \cup \mathcal{V}_M$ then $\mathcal{J}_H = \mathcal{J}_H \cup \{i\}$
 - 4: if $i \in \mathcal{V}_G$ then $\mathcal{J}_P = \mathcal{J}_P \cup \{i\}$
 - 5: if $\exists j \in \mathcal{V}_A \cup \mathcal{V}_M : i \in \mathcal{A}_j$ then $\mathcal{J}_P = \mathcal{J}_P \cup \{i\}$
 - 6: **end for**
-

We note that for this particular setup a sufficient requirement for the heading to be identifiable is that $i \in \mathcal{V}_A \cup \mathcal{V}_M$ (step 3), i.e., that the vehicle has a compass. Furthermore, we see that the position is identifiable either if the vehicle has a GNSS module (step 4) or if it is observed by another vehicle's radar (step 5). Note that without the compass sensor the procedure becomes more involved. For instance the heading of the vehicle is only identifiable through a radar observation against a vehicle with identifiable position.

Given the sets \mathcal{J}_P and \mathcal{J}_H , we can then construct an invertible FIM by removing unidentifiable parameters from $\boldsymbol{\theta}$. Removing a parameter from $\boldsymbol{\theta}$ is equivalent to removing the corresponding rows and columns from the FIM. However, simply removing unidentifiable parameters is equivalent to assuming that these parameters are known, thus we also have to remove measurements that involve these parameters when building up the FIM. The procedure for building up an invertible FIM based on the two sets \mathcal{J}_P and \mathcal{J}_H is summarized in Algorithm 2.

Based on the invertible FIM and the resulting CRLB, it is then straight forward to compute the PEB for the vehicles with identifiable position using (10). For the remaining vehicles, i.e., the vehicles with unidentifiable positions, we simply set the PEB to infinity to represent the fact that we don't have enough information to estimate their position.

Algorithm 2 Build invertible FIM based on \mathcal{J}_P and \mathcal{J}_H

- 1: **for** $i = 1 : N$ **do**
 - 2: if $i \notin \mathcal{J}_H$ then remove ψ_i and $\mathbf{y}_{ij}^R, \forall j \in \mathcal{A}_i$
 - 3: if $i \notin \mathcal{J}_P$ then remove $\mathbf{p}_i, \mathbf{y}_{ij}^R, \forall j \in \mathcal{A}_i$ and $\mathbf{y}_{ji}^R \forall j : i \in \mathcal{A}_j$
 - 4: **end for**
 - 5: Compute FIM for reduced vectors $\boldsymbol{\theta}$ and \mathbf{y} according to the procedure in Section IV-A
-

C. Gain of Cooperation

While the general expression of the FIM provides a mean to assess the PEB numerically, it does not shed insight into the nature of cooperation. Thus, to illustrate the benefits of cooperation, and to get a better understanding what information we gain from the different types of observations we will here illustrate a two vehicle example. To start with we consider two vehicles that observe each other using their respective radars. i.e., the two vehicles are either of type modern or automated and in each others FOV. Moreover, we assume that the two vehicles have similar quality radar sensors and compass sensors, which allows us to drop the index i on σ_C, σ_α and σ_r . Given the sensor models in Section II-B, the resulting FIM can then be expressed as in (14) with matrices

$$\mathbf{A} = \begin{bmatrix} \boldsymbol{\Sigma}_{11}^{-1} + \mathbf{S}_{12} + \mathbf{S}_{21} & -\mathbf{S}_{12} - \mathbf{S}_{21} \\ -\mathbf{S}_{21} - \mathbf{S}_{12} & \boldsymbol{\Sigma}_{22}^{-1} + \mathbf{S}_{12} + \mathbf{S}_{21} \end{bmatrix} \quad (18)$$

$$\mathbf{B} = \begin{bmatrix} \frac{1}{r_{12}\sigma_\alpha^2} \mathbf{R}^T\left(\frac{\pi}{2}\right) \mathbf{u}_{12} & -\frac{1}{r_{21}\sigma_\alpha^2} \mathbf{R}^T\left(\frac{\pi}{2}\right) \mathbf{u}_{21} \\ -\frac{1}{r_{12}\sigma_\alpha^2} \mathbf{R}^T\left(\frac{\pi}{2}\right) \mathbf{u}_{12} & \frac{1}{r_{21}\sigma_\alpha^2} \mathbf{R}^T\left(\frac{\pi}{2}\right) \mathbf{u}_{21} \end{bmatrix} \quad (19)$$

$$\mathbf{C} = \begin{bmatrix} \frac{1}{\sigma_C^2} + \frac{1}{\sigma_\alpha^2} & 0 \\ 0 & \frac{1}{\sigma_C^2} + \frac{1}{\sigma_\alpha^2} \end{bmatrix} \quad (20)$$

The information that the observations carry about the position vector $\mathbf{p} = [\mathbf{p}_1; \mathbf{p}_2]$ as well as the individual positions \mathbf{p}_i for $i = 1, 2$ can then be analyzed with help of the notion of EFI.

For ease of notation and interpretation we introduce the ranging direction matrix (RDM) [28]

$$\mathbf{J}_r(\beta) = \mathbf{u}\mathbf{u}^T, \quad (21)$$

where $\mathbf{u} = [\cos(\beta); \sin(\beta)]$, Furthermore, we let $\gamma = (\frac{1}{\sigma_C^2} + \frac{1}{\sigma_\alpha^2})^{-1}$. The EFIM $\mathbf{J}_e(\mathbf{p})$ for the position vector $\mathbf{p} = [\mathbf{p}_1; \mathbf{p}_2]$ can then be determined as follows.

Proposition 2. *For the scenario with two modern or automated vehicles in each-other's FOV, the EFIM for the position vector \mathbf{p} can be expressed as*

$$\mathbf{J}_e(\mathbf{p}) = \begin{bmatrix} \boldsymbol{\Sigma}_{11}^{-1} + \mathbf{H} & -\mathbf{H} \\ -\mathbf{H} & \boldsymbol{\Sigma}_{22}^{-1} + \mathbf{H} \end{bmatrix}, \quad (22)$$

where $\mathbf{H} = \mathbf{S}_{12} + \mathbf{S}_{21} - \gamma\mathbf{E}$, and

$$\mathbf{E} = \frac{2}{r^2\sigma_\alpha^4} \mathbf{J}_r(\beta' + \frac{\pi}{2}), \quad (23)$$

in which $r = r_{12} = r_{21}$, and β' is either β_{12} or β_{21} .

Proof: See Appendix B. ■

We observe that in (22), the diagonal elements corresponds to the information about \mathbf{p}_1 (resp. \mathbf{p}_2) given that \mathbf{p}_2 (resp. \mathbf{p}_1)

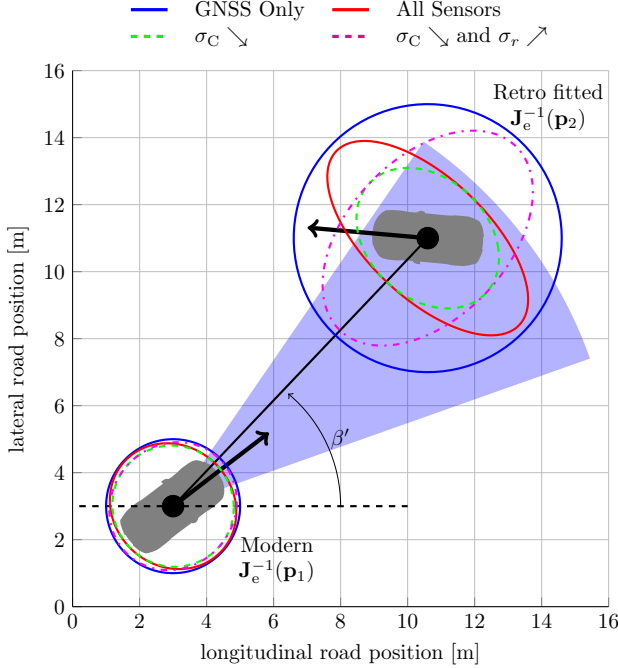


Figure 1. Illustration of 1-sigma ellipses representing the CRLBs $\mathbf{J}_e^{-1}(\mathbf{p}_1)$ and $\mathbf{J}_e^{-1}(\mathbf{p}_2)$ for a two vehicle scenario with a modern vehicle with position \mathbf{p}_1 and a retrofitted vehicle with position \mathbf{p}_2 . First we see the uncertainty in the positions given that we only take into account the GNSS measurements (solid blue). Then we see how the uncertainty changes when incorporating the radar ($\sigma_\alpha = 0.3$ and $\sigma_r = 0.12$) as well as the compass ($\sigma_C = 1$) from the modern vehicle (solid red). We also see how the uncertainty about the retrofitted vehicle decreases in the direction $\beta' + \pi/2$ when decreasing the uncertainty in the modern vehicles compass to $\sigma_C = 0.2^\circ$ (dashed green), and how the uncertainty about the retrofitted vehicle is increased in the direction β' if we in addition increase the range uncertainty of the radar to $\sigma_r = 12$ (dashed magenta). Note that parameter values used here might differ from Section V.

is known. We note that each diagonal element contains information from the own GNSS measurement plus \mathbf{H} , which correspond to the information from the cooperation with the other vehicle. Further analyzing the structure of the matrix \mathbf{H} , we see that the cooperation with the other vehicle adds information $\mathbf{S}_{12} + \mathbf{S}_{21}$, but due to the uncertainty in the headings of the vehicles this information is reduced by the matrix $\gamma\mathbf{E}$. In particular, we see from the structure of \mathbf{E} that uncertainties in the angles translates to a reduction of information in the direction $\beta' + \frac{\pi}{2}$, which is in the direction perpendicular to the direction between the two nodes.

Further applying the notion of EFI, we can compute the EFIM for the position of vehicle $i = 1$. The resulting expression is presented in Proposition 3

Proposition 3. *For the two vehicle example with an EFIM for the complete position vector \mathbf{p} as in (22), the EFIM for the position of vehicle $i = 1$ can be expressed as*

$$\mathbf{J}_e(\mathbf{p}_1) = \sigma_{G,1}^{-2} \mathbf{I}_2 + \kappa_1 \lambda_1^{\mathbf{H}} \mathbf{J}_r(\beta') + \kappa_2 \lambda_2^{\mathbf{H}} \mathbf{J}_r(\beta' + \frac{\pi}{2}) \quad (24)$$

where $\kappa_n = 1 - \lambda_n^{\mathbf{H}} / (\lambda_n^{\mathbf{H}} + 1 / \sigma_{G,2}^2)$, $\lambda_1^{\mathbf{H}} = \frac{2}{\sigma_r^2}$, $\lambda_2^{\mathbf{H}} = \frac{2}{r^2} (\frac{1}{\sigma_\alpha^2} - \frac{\gamma}{\sigma_\alpha^4})$, and β' is either $\beta_{12} =$ or β_{21} .

Proof: See Appendix C. ■

We observe that information is gained in two directions β' and $\beta' + \pi/2$, where β' correspond to the direction towards \mathbf{p}_2 . The amount of information that we gain in the two directions are $\kappa_1 \lambda_1^{\mathbf{H}}$ and $\kappa_2 \lambda_2^{\mathbf{H}}$. Furthermore, we see that as the GNSS observation variance $\sigma_{G,2}^2$ tends to zero, κ_n tends to one, and that while $\sigma_{G,2}^2$ tends to infinity, κ_n tends to zero. In other words, $\lambda_1^{\mathbf{H}}$ and $\lambda_2^{\mathbf{H}}$ correspond to the information gain given that \mathbf{p}_2 is known, while κ_n can be seen as a dampening factor due to uncertainties in the other vehicle's position. We also see that when $\kappa_n = 1$, the information gain in the direction towards the other vehicle is inversely proportional to σ_r^2 , while the information gain in the perpendicular direction depends on both σ_α^2 and σ_C^2 , as well as the distance between the two vehicles.

Remark 4. If one of the vehicle is not in the FOV of the other, or if the the type of one of the vehicles is changed to retrofitted a slight modification of Proposition 3 is required. In this case the eigenvalues $\lambda_1^{\mathbf{H}}$ and $\lambda_2^{\mathbf{H}}$ are reduced by 50% as only one radar observation is available. Changing the type of the first vehicle to a legacy vehicle, i.e., no GNSS observation requires both the 50% reduction of the eigenvalues as well as a removal of the first term in (24). Finally, changing the second vehicle into a legacy vehicle the EFIM $\mathbf{J}_e(\mathbf{p}_1)$ is simply $\frac{1}{\sigma_{G,1}^2} \mathbf{I}_2$, which can be seen by letting the GNSS observation variance of the second vehicle tend to infinity.

To give further intuition behind Proposition 3 and how different type of observations affects the EFIMs of the individual vehicles, Fig. 1 visualizes 1-sigma ellipses representing the CRLBs $\mathbf{J}_e^{-1}(\mathbf{p}_1)$ and $\mathbf{J}_e^{-1}(\mathbf{p}_2)$ for a case with a modern and a retrofitted vehicle. To get a more illustrative example, we have set the accuracy of their respective GNSS modules to $\sigma_{G,1} = 2$ m and $\sigma_{G,2} = 4$ m. In other words, based on GNSS only, we are more uncertain about the retrofitted vehicles position. This can be seen by comparing the size of the blue ellipses, which correspond to the CRLBs based on solely GNSS measurements. Incorporating radar and compass measurements (with $\sigma_r = 0.12$ m, $\sigma_\alpha = 0.3^\circ$ and $\sigma_C = 1^\circ$), we obtain the red ellipses. From these we see that adding radar and compass marginally decreases the uncertainty about the modern vehicles position, but significantly decreases the uncertainty about the retrofitted vehicles position, especially in the direction towards the other vehicle (i.e., along the direction β'). That the uncertainty is decreased most for the retrofitted vehicle is reasonable, as the relative radar measurement allows for information transfer from the modern vehicle with good GNSS to the retrofitted vehicle with bad GNSS. Because of the comparatively low range uncertainty it is also intuitive that the uncertainty is reduced most in the direction towards the other vehicle. Note that even though the uncertainty is reduced mostly in the direction β' , we also see a slight reduction in the perpendicular direction (i.e., $\beta' + \pi/2$). As visualized by the green ellipses, the reduction in the perpendicular direction becomes more pronounced if decreasing the standard deviation of the compass sensor to $\sigma_C = 0.2^\circ$, i.e., if we better know the direction of the modern vehicle with radar we can transfer more information in the direction $\beta' + \pi/2$. Finally, if we

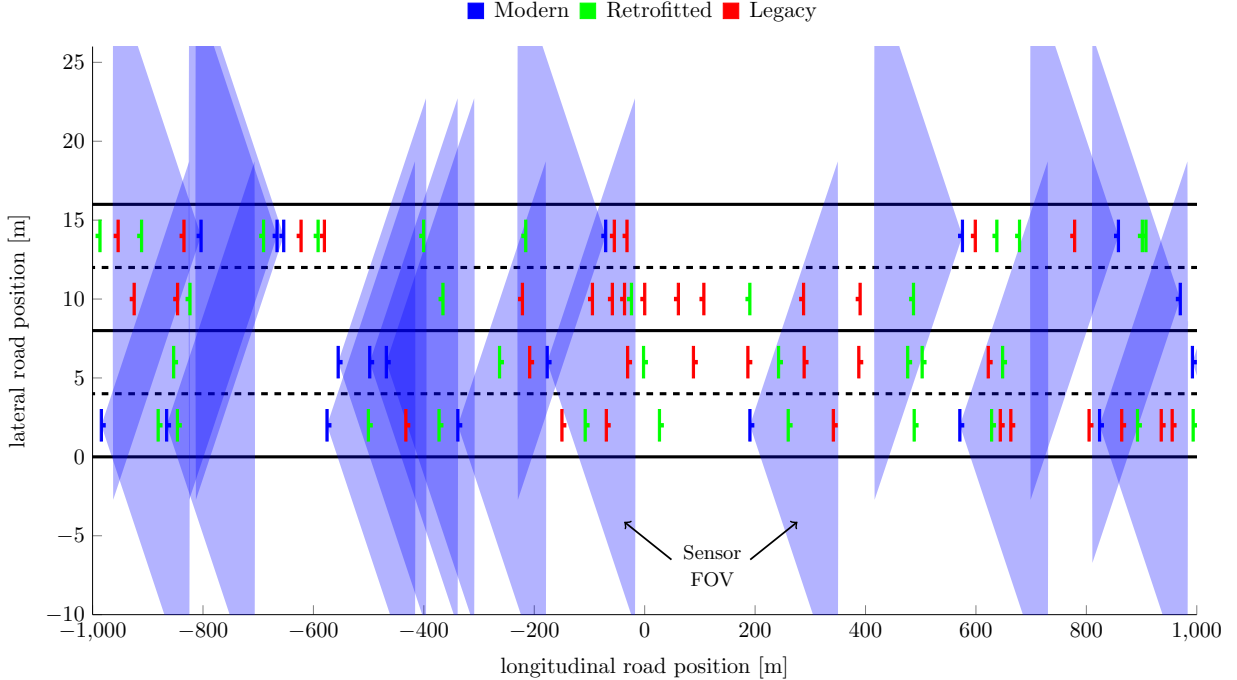


Figure 2. Illustration of one network realization showing node deployment, type assignment and sensor coverage for the radars in the modern vehicles. The fraction of vehicles used for the multinomial sampling are in this example set to $\rho = [0, 0.25, 0.4, 0.35]$.

in addition to decreasing the compass standard deviation also increase the range uncertainty of the radar to $\sigma_r = 12$, we obtain the magenta colored ellipses. As can be seen, this results in a increased uncertainty in the direction β' , compared to the case with low range uncertainty.

V. NUMERICAL RESULTS

A. Simulation Setup

We consider a multi-lane freeway of length $L = 2$ km, which has two lanes in each direction. The width of the lanes $d_{\text{lane}} = 4$ m, and when it comes to the lateral placement of vehicles within a lane, we assume that vehicles are placed exactly along the centerline of each lane. For the longitudinal placement of vehicles, experimental studies have shown that for free flow traffic the distribution of time headways (i.e. the time between successive vehicles) is well approximated by a log normal distribution [34]–[36]. Thus we generate the longitudinal positions of the vehicles in each lane by drawing time headway samples from a log-normal distribution with parameters μ' and σ' . The specific values of μ' and σ' are shown in Table I, and are chosen to match one of the cases from the multi-lane freeway study in [34]. The time headways are converted to headway distances by assuming a velocity of $v = 100$ km/h. After deploying vehicles in each lane we assign a type T_i to each vehicle. This is done by drawing independent samples from a multinomial distribution with parameter $\rho = [\rho_A \ \rho_M \ \rho_R \ \rho_L]$. For the sensor parameters we set the uncertainty of the high-accuracy and low-cost receivers to $\sigma_G^{\text{high}} = 0.05$ m and $\sigma_G^{\text{low}} = 2$ m, respectively [10], [37]. The uncertainty of the compass sensor

is set to $\sigma_C = 1^\circ$. Furthermore, we assume that the radars in the automated vehicles have a maximum detection range of $r_{\text{max}} = 160$ m and opening angle $\theta_{\text{FOV}}^A = 360^\circ$, while the radars in the modern vehicles are assumed to be front looking radars with the same maximum detection range but an opening angle $\theta_{\text{FOV}}^M = 12^\circ$. The range and bearing uncertainty of both radar types are set to $\sigma_r = 0.12$ m $\sigma_\alpha = 0.3^\circ$. Note that the values for the front looking radar approximately match the specification of a typical medium range radar [38]. One realization of the generated network can be seen in Fig. 2, which in addition to the node deployment and type assignment also visualizes the sensor coverage for the radar sensors. Note that in regards to the radar observations, we assume that vehicles can observe all other vehicles within the sensor FOV, including both oncoming traffic and traffic traveling in the same direction. Finally, to minimize the impact of edge effects we place a replica of the generated network before and after the 2 km long freeway stretch that we want to analyze. Based on the generated network we then compute the adjacency sets and measurement covariances required to set up the complete network FIM and compute the CRLB and corresponding PEB for each vehicles position.

B. Results and Discussion

The impact of the gradual market penetration, and the possibility to build up a common shared map in the multi-lane freeway scenario introduced in Section V-A is here evaluated by running a set of Monte Carlo simulations. For each parameter setting we draw 1600 realizations of the network, and in particular we focus on how the fraction of vehicles that can

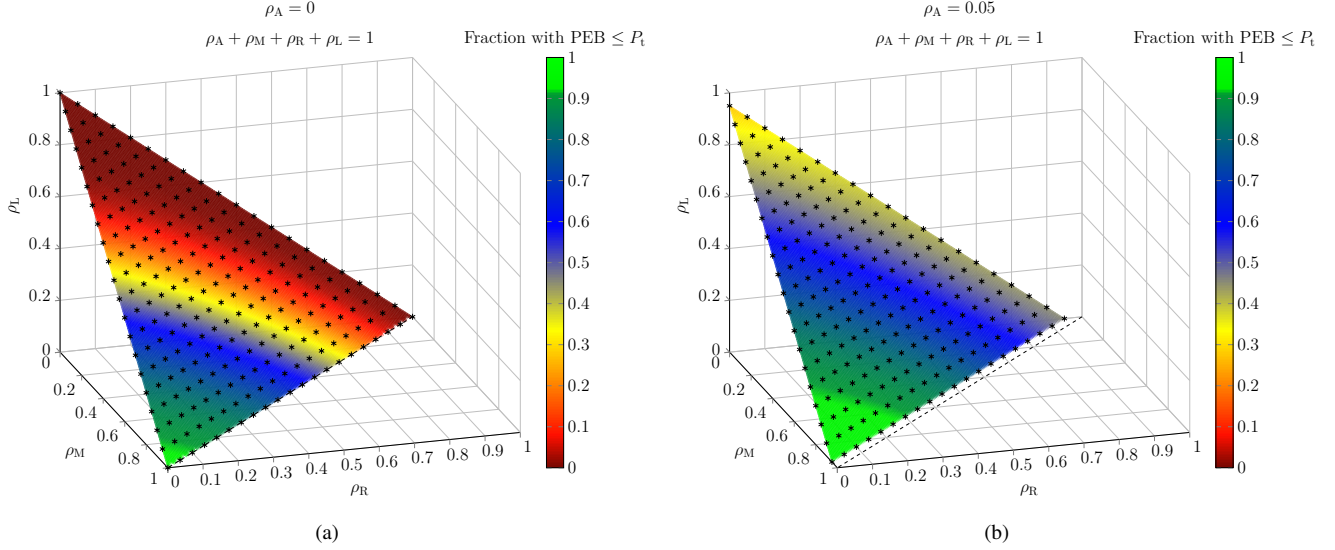


Figure 3. Fraction of vehicles with a PEB below or equal to $P_t = 1$ m as a function of the fraction of modern, retrofitted and legacy vehicles in the system when (a) the fraction automated vehicles $\rho_A = 0$, and (b) the fraction of automated vehicles is $\rho_A = 0.05$. The black stars represents the grid points for which simulations have been run.

Table I
SIMULATION PARAMETERS

Parameters	Values
Length of road segment (km)	$L = 2$
Width of lane (m)	$d_{\text{lane}} = 4$
Time headway mean (m)	$\mu^l = 0.886$
Time headway std. (m)	$\sigma^l = 0.954$
Speed (km/h)	$v = 100$
GNSS position unc. high-accuracy (m)	$\sigma_G^{\text{high}} = 0.05$
GNSS position unc. low-cost (m)	$\sigma_G^{\text{low}} = 2$
Compass heading unc. (deg)	$\sigma_C = 1$
Radar opening angle automated veh. (deg)	$\theta_{\text{FOV}}^A = 360$
Radar opening angle modern veh. (deg)	$\theta_{\text{FOV}}^M = 12$
Radar max range (m)	$r_{\text{max}} = 160$
Radar range unc. (m)	$\sigma_r = 0.12$
Radar bearing unc. (deg)	$\sigma_\alpha = 0.3$

meet a certain target accuracy depends on the composition of the vehicle fleet $\boldsymbol{\rho} = [\rho_A \ \rho_M \ \rho_R \ \rho_L]$. Some of the questions that we will try to answer are: How sensitive are the results to the chosen target accuracy? What is the impact of adding a small fraction of automated vehicles to the system, and is this sufficient to reach the accuracies required for safety critical ITS applications? What is the effect of relatively simple and cheap measures such as retrofitting vehicles with low-cost GNSS and communication? Is there a difference between longitudinal and lateral estimation accuracy?

1) Impact of Penetration Rates and Different Requirements:

To answer these question, we start by visualizing how the fraction of vehicles that can meet a fixed target accuracy of $P_t = 1$ m depends on $\boldsymbol{\rho} = [\rho_A \ \rho_M \ \rho_R \ \rho_L]$. While Fig. 3a shows the case when there are no automated vehicles in the system, Fig. 3b shows results for a case where we have introduced 5% automated vehicles in the system. From Fig. 3, which provides a good overview of how the composition of the vehicle fleet affects the results, we see that increasing the

density of modern vehicles ρ_M in the system generally leads to an increase in the fraction of vehicles that can achieve the target accuracy. Furthermore, we see that when there are only legacy vehicles without sensing capability in the network (i.e. $\rho_L = 1$), the target can not be met for any vehicles. We also see that converting legacy vehicles into retrofitted vehicles, in most cases intuitively allows us to meet the target accuracy for a larger fraction of vehicles. However, note that when there are solely retrofitted vehicles in the system (i.e., $\rho_R = 1$) the target accuracy can not be met for any of the vehicles in the system, this is because the accuracy of the low-cost GNSS module is not sufficient to achieve a target accuracy of 1 m. Furthermore, we clearly see the benefit of introducing a small fraction of automated vehicles with high-end sensors, as this generally leads to a significant increase in the fraction of vehicles for which the target accuracy can be met.

To better quantify the effect of adding a small fraction of automated vehicles, and to analyze the impact of different positioning requirements, Fig. 4 shows the fraction of vehicles that can meet the requirement as a function of the fraction of modern vehicles ρ_M for different target accuracies $P_t \in \{0.5 \text{ m}, 1 \text{ m}, 3 \text{ m}\}$. For visualization purposes, we have here fixed the fraction of retrofitted vehicles to $\rho_R = 0$. As expected, we observe that the number of vehicles that can meet the target decreases with a decreased target accuracy. We also more clearly see that introducing 5% automated vehicles, leads to a significant increase in the fraction of vehicles for which we can meet the target. However, as can be seen, this alone is not sufficient if we want to get down to the tens of centimeters required for safety critical applications. At least not given the current sensor configurations, and under the assumption that we would like to position all the vehicles in the system with this accuracy. Furthermore, we see that in contrast to the immediate benefits of adding a small fraction of automated vehicles, we have a delayed and accelerating effect

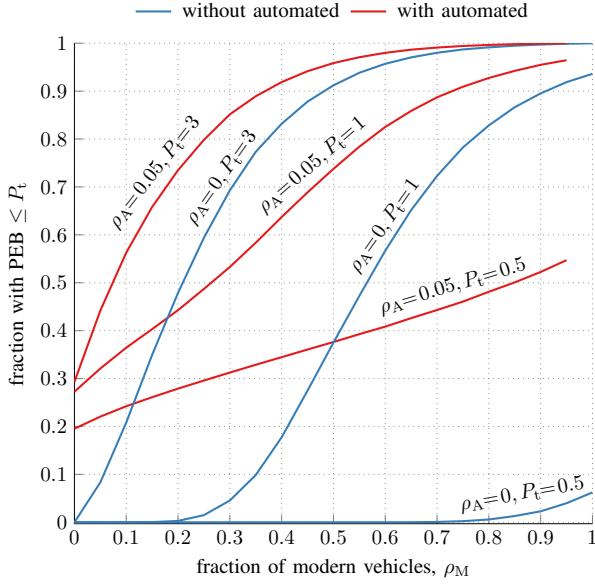


Figure 4. Fraction of vehicles with $\text{PEB} \leq P_t \in \{0.5 \text{ m}, 1 \text{ m}, 3 \text{ m}\}$ as a function of the fraction of modern vehicles ρ_M in the system. The fraction of retrofitted vehicles is set to $\rho_R = 0$. Blue curves correspond to the case without automated vehicles (i.e., $\rho_A = 0$) and red curves to the case with automated vehicles (i.e., $\rho_A = 0.05$).

of adding more modern vehicles to the system for the case without automated vehicles. For instance, when $P_t = 1$ the benefit of having 20% modern vehicles in the system is almost negligible, but after this the fraction of vehicles for which the target can be met rapidly increases as we increase ρ_M . To gain a better understanding about the sensitivity to different positioning requirements Fig. 5 shows empirical CDFs of the PEB. Each CDF correspond to a particular ρ , and for visualization purposes we have chosen to fix the fraction of retrofitted vehicles to $\rho_R = 0.2$. To start with, we observe that the CDFs are steeper for low PEBs and then flatten out. We also note that there are a few steps on the CDFs. These steps occur because of (i) some vehicles can only be positioned based on information from their on-board GNSS receivers; (ii) certain types of vehicle configurations are more common and reoccur in combination with that σ_r is assumed to be independent of the distance between two vehicles. This means that the results are more sensitive to a change in target accuracy when the target accuracy is low, i.e. when the CDFs are steep, or when the selected target accuracy is close to one of the steps.

2) *Effect of Retrofitting Vehicles:* To analyze what effects the relatively simple solution of retrofitting vehicles with a low-cost GNSS and communication, Fig. 6 shows the fraction of vehicles that meet the target as a function of the fraction of retrofitted vehicles ρ_R . From this figure we see that only when we have loose position requirements (such as $P_t = 3$ m), which can be met by the low-cost GNSS module alone, the benefit of this relatively simple measure is clear. However, as can be seen from the flat or relatively flat curves corresponding to $P_t \in \{0.5 \text{ m}, 1 \text{ m}\}$, there is from a mapping perspective none or marginal benefit of introducing more retrofitted vehicles if the positioning requirements on the LDM are stringent.

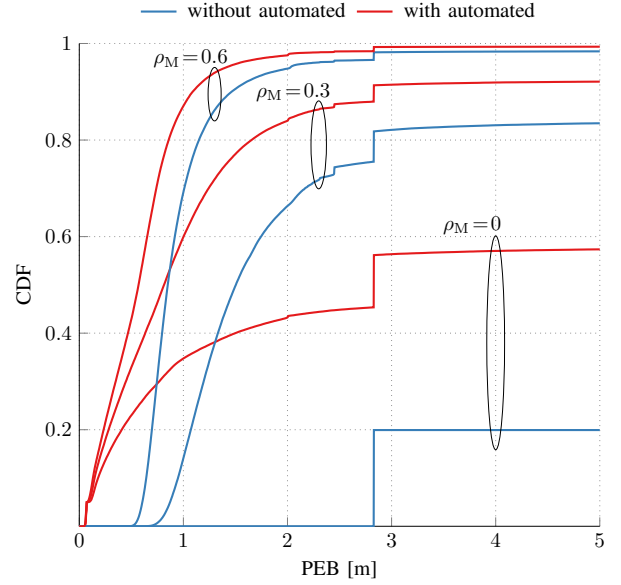


Figure 5. Empirical CDFs of the PEB for $\rho_A \in \{0, 0.05\}$, $\rho_M \in \{0, 0.3, 0.6\}$, $\rho_R = 0.2$, and $\rho_L = 1 - \rho_A - \rho_M - \rho_R$. Blue curves correspond to the case without automated vehicles (i.e., $\rho_A = 0$) and red curves to the case with automated vehicles (i.e., $\rho_A = 0.05$).

3) *Longitudinal vs Lateral Error:* Finally, we distinguish between lateral and longitudinal road position. Fig. 7 shows the fraction of vehicles that can meet the target accuracy for the individual components as a function of the fraction of modern vehicles ρ_M . For visualization purposes, we have as before set the fraction of retrofitted vehicles to $\rho_R = 0$. From this figure we see that in general a larger fraction of the vehicles manages to meet the requirement in the longitudinal component compared to the lateral, even though the difference in the fraction of vehicles that can meet the requirement seems to be larger for more stringent positioning requirements. Nonetheless, given the current sensor configuration, it is clear that longitudinal road position can be estimated more accurately in a multi-lane highway scenario.

VI. CONCLUSIONS

Accurate positioning and real-time situational awareness are key enablers in future ITS. In this paper, we present a framework and methodology, based on Fisher information analysis and Cramér-Rao bounds, that can be used to analyze how the sensing capability in a given vehicle fleet affects the possibility to build up a shared LDM in which both cooperative and non-cooperative vehicles are positioned. We have used this, to study how the composition of the vehicle fleet, and its sensing capability, affects the quality of the LDM in terms of the PEB of the involved vehicles. More specifically, we have quantified the information gain from different type of observations (such as GNSS, compass and radar), and showed how the fraction of vehicles that can meet a certain target accuracy depends on the sensing capability in the network. While the framework and methodology is general and can be applied to any network of vehicles, we present simulation results for a multi-lane freeway scenario with mixed traffic,

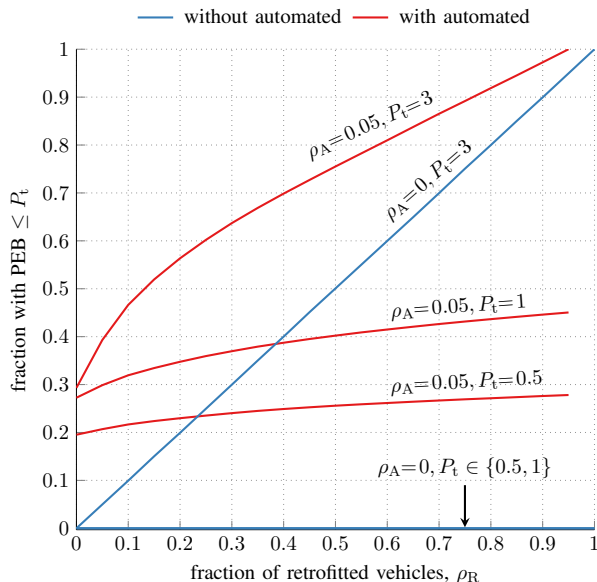


Figure 6. Fraction of vehicles with $\text{PEB} \leq P_t \in \{0.5 \text{ m}, 1 \text{ m}, 3 \text{ m}\}$ as a function of the fraction of retrofitted vehicles ρ_R in the system. The fraction of modern vehicles is set to $\rho_M = 0$. Blue curves correspond to the case without automated vehicles (i.e., $\rho_A = 0$) and red curves to the case with automated vehicles (i.e., $\rho_A = 0.05$).

consisting of four vehicle types ranging from legacy vehicles with neither sensing nor communication, to automated vehicles with high-end sensors and communication capability. The insights that we can obtain from these simulations, are that solely introducing a small fraction of automated vehicles significantly improves the positioning quality in the network. However, it might not be sufficient if we want to achieve a target accuracy corresponding to the tens of centimeters required for safety critical ITS applications (such as cooperative automated driving). Furthermore, we find that simple measures such as retrofitting vehicles with low-cost GNSS and communication have marginal impact when the positioning requirements on the LDM are stringent, and that longitudinal road position can be estimated more accurately than lateral in a multi-lane highway scenario, given the considered sensor configuration.

Possible avenues for future research include: (i) incorporation of realistic model for sensor blockage, such that measurements against vehicles that in reality are occluded behind other vehicles can be excluded from the analysis; (ii) extension to dynamic scenarios with tracking, as any realistic implementation of a cooperative positioning algorithm most likely would rely on tracking; (iii) incorporation of advanced sensor models and extended objects to model the fact that vehicles in reality are not point objects, and can give rise to more than one measurement per vehicle if high resolution sensors are used.

APPENDIX A PROOF OF PROPOSITION 1

For a vector of unknown parameters $\boldsymbol{\theta} = [\boldsymbol{\theta}_1; \dots; \boldsymbol{\theta}_K]$ and a joint Gaussian measurement likelihood (as in (2)) with mean function of the form $\mathbf{f}(\boldsymbol{\theta}) = [\mathbf{f}_1; \dots; \mathbf{f}_M]$ and corresponding

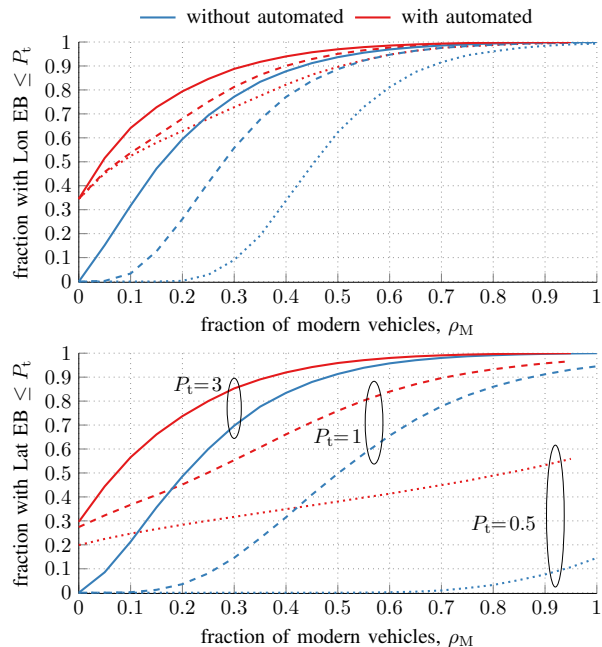


Figure 7. Fraction of vehicles with with longitudinal error bound (Lon EB) and lateral error bound (Lat EB) that meets the target accuracy $P_t \in \{0.5 \text{ m}, 1 \text{ m}, 3 \text{ m}\}$ as a function of the fraction of modern vehicles ρ_M . The fraction of retrofitted vehicles is set to $\rho_R = 0$. Blue curves correspond to the case with no automated vehicles (i.e., $\rho_A = 0$) and red curves to the case with automated vehicles (i.e., $\rho_A = 0.05$). Solid, dashed and dotted lines correspond to target accuracies of $P_t = 3 \text{ m}$, $P_t = 1 \text{ m}$ and $P_t = 0.5 \text{ m}$, respectively.

block diagonal covariance $\boldsymbol{\Sigma}$, a general block in $\mathbf{J}(\boldsymbol{\theta})$ can be expressed as

$$[\mathbf{J}(\boldsymbol{\theta})]_{i,j} = \frac{\partial^T \mathbf{f}(\boldsymbol{\theta})}{\partial \boldsymbol{\theta}_i} \boldsymbol{\Sigma}^{-1} \frac{\partial \mathbf{f}(\boldsymbol{\theta})}{\partial \boldsymbol{\theta}_j} \quad (25)$$

$$= \sum_{n=1}^M \frac{\partial^T \mathbf{f}_n}{\partial \boldsymbol{\theta}_i} \boldsymbol{\Sigma}_n^{-1} \frac{\partial \mathbf{f}_n}{\partial \boldsymbol{\theta}_j} \quad (26)$$

where $\boldsymbol{\Sigma}_n$ denotes the covariance corresponding to mean function \mathbf{f}_n . We observe that information is additive, and that a particular measurement only contributes when both of the partial derivatives are non zero. It should be understood that the exact dimension of the block $[\mathbf{J}(\boldsymbol{\theta})]_{i,j}$ depends on the size of $\boldsymbol{\theta}_i$ as well as $\boldsymbol{\theta}_j$. For the specific setting considered here, $\boldsymbol{\theta}_i$'s are either two dimensional positions \mathbf{p}_i or one dimensional headings ψ_i . The way $\boldsymbol{\theta}$ is composed in (11), further allows us to structure the FIM as in (14), where the matrix \mathbf{A} is a $2N \times 2N$ matrix consisting of blocks $[\mathbf{J}(\boldsymbol{\theta})]_{i,j}$ for $\boldsymbol{\theta}_i, \boldsymbol{\theta}_j \in \{\mathbf{p}_1, \dots, \mathbf{p}_N\}$, \mathbf{B} is a $2N \times N$ matrix consisting of blocks $[\mathbf{J}(\boldsymbol{\theta})]_{i,j}$ for $\boldsymbol{\theta}_i \in \{\mathbf{p}_1 \dots \mathbf{p}_N\}$ and $\boldsymbol{\theta}_j \in \{\psi_1 \dots \psi_N\}$, and \mathbf{C} is a $N \times N$ matrix consisting of blocks $[\mathbf{J}(\boldsymbol{\theta})]_{i,j}$ for $\boldsymbol{\theta}_i, \boldsymbol{\theta}_j \in \{\psi_1 \dots \psi_N\}$. Given the sensor models in Section II-B, the non-zero partial derivatives required to evaluate the different blocks are

$$\frac{\partial \mathbf{f}_{ii}^G(\mathbf{x}_i, \mathbf{x}_i)}{\partial \mathbf{p}_i} = \frac{\partial \mathbf{p}_i}{\partial \mathbf{p}_i} = \mathbf{I}_2 \quad (27)$$

$$\frac{\partial f_{ii}^C(\mathbf{x}_i, \mathbf{x}_i)}{\partial \psi_i} = \frac{\partial \psi_i}{\partial \psi_i} = 1 \quad (28)$$

$$\frac{\partial \mathbf{f}_{ij}^R(\mathbf{x}_i, \mathbf{x}_j)}{\partial \mathbf{p}_i} = \frac{\partial \mathbf{R}(\psi_i)(\mathbf{p}_j - \mathbf{p}_i)}{\partial \mathbf{p}_i} = -\mathbf{R}(\psi_i) \quad (29)$$

$$\frac{\partial \mathbf{f}_{ij}^R(\mathbf{x}_i, \mathbf{x}_j)}{\partial \mathbf{p}_j} = \frac{\partial \mathbf{R}(\psi_i)(\mathbf{p}_j - \mathbf{p}_i)}{\partial \mathbf{p}_j} = \mathbf{R}(\psi_i) \quad (30)$$

$$\frac{\partial f_{ij}^R(\mathbf{x}_i, \mathbf{x}_j)}{\partial \psi_i} = \frac{\partial \mathbf{R}(\psi_i)(\mathbf{p}_j - \mathbf{p}_i)}{\partial \psi_i} = \boldsymbol{\mu}_{ij} \quad (31)$$

where we for ease of notation have introduced $\boldsymbol{\mu}_{ij} = \mathbf{R}(\psi_i + \pi/2)(\mathbf{p}_j - \mathbf{p}_i)$.

Based on this we can now express a general 2×2 block in \mathbf{A} as

$$[\mathbf{A}]_{i,j} = \sum_{n=1}^M \frac{\partial^T \mathbf{f}_n}{\partial \mathbf{p}_i} \boldsymbol{\Sigma}_n^{-1} \frac{\partial \mathbf{f}_n}{\partial \mathbf{p}_j}. \quad (32)$$

where inserting the exact exact form of the mean functions and evaluating the partial derivatives results in diagonal and off-diagonal blocks

$$\begin{aligned} [\mathbf{A}]_{i,i} &= 1_{\{i \in \mathcal{V}_G\}} \boldsymbol{\Sigma}_{ii}^{-1} + \sum_{j \in \mathcal{A}_i} \mathbf{R}^T(\psi_i) \boldsymbol{\Sigma}_{ij}^{-1} \mathbf{R}(\psi_i) \\ &+ \sum_{j: i \in \mathcal{A}_j} \mathbf{R}^T(\psi_j) \boldsymbol{\Sigma}_{ji}^{-1} \mathbf{R}(\psi_j) \end{aligned} \quad (33)$$

and

$$\begin{aligned} [\mathbf{A}]_{i,j} &= -1_{\{j \in \mathcal{A}_i\}} \mathbf{R}^T(\psi_i) \boldsymbol{\Sigma}_{ij}^{-1} \mathbf{R}(\psi_i) \\ &- 1_{\{i \in \mathcal{A}_j\}} \mathbf{R}^T(\psi_j) \boldsymbol{\Sigma}_{ji}^{-1} \mathbf{R}(\psi_j). \end{aligned} \quad (34)$$

Introducing $\mathbf{S}_{ij} = \mathbf{R}^T(\psi_i) \boldsymbol{\Sigma}_{ij}^{-1} \mathbf{R}(\psi_i)$ leads to (15).

Similarly, for the matrix \mathbf{B} we can write the 2×1 blocks as

$$[\mathbf{B}]_{i,j} = \sum_{n=1}^M \frac{\partial^T \mathbf{f}_n}{\partial \mathbf{p}_i} \boldsymbol{\Sigma}_n^{-1} \frac{\partial \mathbf{f}_n}{\partial \psi_j}. \quad (35)$$

Again, inserting the exact form of the mean functions and evaluating the partial derivatives gives diagonal and off-diagonal blocks

$$[\mathbf{B}]_{i,i} = - \sum_{j \in \mathcal{A}_i} \mathbf{R}^T(\psi_i) \boldsymbol{\Sigma}_{ij}^{-1} \boldsymbol{\mu}_{ij} \quad (36)$$

and

$$[\mathbf{B}]_{i,j} = 1_{\{i \in \mathcal{A}_j\}} \mathbf{R}^T(\psi_j) \boldsymbol{\Sigma}_{ji}^{-1} \boldsymbol{\mu}_{ji}. \quad (37)$$

As can be seen, the diagonal and off diagonal blocks contains terms of the form

$$\mathbf{T}_{ij} = \mathbf{R}^T(\psi_i) \boldsymbol{\Sigma}_{ij}^{-1} \boldsymbol{\mu}_{ij} \quad (38)$$

$$= \mathbf{R}^T(\psi_i) \boldsymbol{\Sigma}_{ij}^{-1} \mathbf{R}(\psi_i + \pi/2)(\mathbf{p}_j - \mathbf{p}_i). \quad (39)$$

The vector $(\mathbf{p}_j - \mathbf{p}_i)$ can be written as $r_{ij} \mathbf{u}_{ij}$, with $\mathbf{u}_{ij} = [\cos(\beta_{ij}); \sin(\beta_{ij})]$ in which $\beta_{ij} = \psi_i + \alpha_{ij}$. Using this

in combination with the expression for the radar covariance in (5), we can write

$$\mathbf{T}_{ij} = r_{ij} \mathbf{R}^T(\psi_i) \mathbf{R}^T(\alpha_{ij}) (\boldsymbol{\Sigma}_{ij}^{P*})^{-1} \mathbf{v} \quad (40)$$

where $\mathbf{v} = \mathbf{R}(\alpha_{ij}) \mathbf{R}(\psi_i) \mathbf{R}(\frac{\pi}{2}) \mathbf{u}_{ij}$. As the vector $\mathbf{v} = [0; -1]$ for all α_{ij} and ψ_{ij} , we can further express these terms as

$$\mathbf{T}_{ij} = r_{ij} \mathbf{R}^T(\beta_{ij}) (\boldsymbol{\Sigma}_{ij}^{P*})^{-1} \begin{bmatrix} 0 \\ -1 \end{bmatrix} \quad (41)$$

$$= r_{ij} \mathbf{R}^T(\beta_{ij}) \begin{bmatrix} \frac{1}{\sigma_{r,i}^2} & 0 \\ 0 & \frac{1}{(r_{ij} \sigma_{\alpha,i})^2} \end{bmatrix} \begin{bmatrix} 0 \\ -1 \end{bmatrix} \quad (42)$$

$$= \frac{1}{r_{ij} \sigma_{\alpha,i}^2} \mathbf{R}^T\left(\frac{\pi}{2}\right) \mathbf{u}_{ij} \quad (43)$$

Plugging the final result for \mathbf{T}_{ij} back into (36)-(37) leads to (16).

Finally for the matrix \mathbf{C} we can write the elements as

$$[\mathbf{C}]_{i,j} = \sum_{n=1}^M \frac{\partial^T \mathbf{f}_n}{\partial \psi_i} \boldsymbol{\Sigma}_n^{-1} \frac{\partial \mathbf{f}_n}{\partial \psi_j}. \quad (44)$$

As before inserting the exact mean functions and evaluating the partial derivatives we see that the only non-zero elements are the diagonal elements, which can be written as

$$[\mathbf{C}]_{i,i} = 1_{\{i \in \mathcal{V}_A \cup \mathcal{V}_M\}} \frac{1}{\sigma_{C,i}^2} + \sum_{j \in \mathcal{A}_i} \boldsymbol{\mu}_{ij}^T \boldsymbol{\Sigma}_{ij}^{-1} \boldsymbol{\mu}_{ij} \quad (45)$$

Again using that the vector $(\mathbf{p}_j - \mathbf{p}_i) = r_{ij} \mathbf{u}_{ij}$, we can for a radar covariance of the form in (5) finally write

$$\begin{aligned} [\mathbf{C}]_{i,i} &= 1_{\{i \in \mathcal{V}_A \cup \mathcal{V}_M\}} \frac{1}{\sigma_{C,i}^2} + \sum_{j \in \mathcal{A}_i} r_{ij}^2 \mathbf{v}^T (\boldsymbol{\Sigma}_{ij}^{P*})^{-1} \mathbf{v} \end{aligned} \quad (46)$$

$$= 1_{\{i \in \mathcal{V}_A \cup \mathcal{V}_M\}} \frac{1}{\sigma_{C,i}^2} + \sum_{j \in \mathcal{A}_i} \frac{1}{\sigma_{\alpha,i}^2}, \quad (47)$$

which by combined with the zero valued off-diagonals leads to (17)

APPENDIX B PROOF OF PROPOSITION 2

Based on the matrices in (18)-(20), we can express the EFIM for the position vector \mathbf{p} as

$$\mathbf{J}_e(\mathbf{p}) = \mathbf{A} - \mathbf{B}\mathbf{C}^{-1}\mathbf{B}^T \quad (48)$$

$$= \mathbf{A} - \gamma \mathbf{B}\mathbf{B}^T \quad (49)$$

where $\gamma = (\frac{1}{\sigma_C^2} + \frac{1}{\sigma_\alpha^2})^{-1}$. We can then write $\mathbf{B}\mathbf{B}^T$ as

$$\mathbf{B}\mathbf{B}^T = \begin{bmatrix} \mathbf{E} & -\mathbf{E} \\ -\mathbf{E} & \mathbf{E} \end{bmatrix}. \quad (50)$$

with

$$\mathbf{E} = \frac{1}{r_{12}^2 \sigma_\alpha^4} \mathbf{R}^T\left(\frac{\pi}{2}\right) \mathbf{u}_{12} \mathbf{u}_{12}^T \mathbf{R}\left(\frac{\pi}{2}\right) \quad (51)$$

$$+ \frac{1}{r_{21}^2 \sigma_\alpha^4} \mathbf{R}^T\left(\frac{\pi}{2}\right) \mathbf{u}_{21} \mathbf{u}_{21}^T \mathbf{R}\left(\frac{\pi}{2}\right) \quad (52)$$

$$= \frac{1}{r^2 \sigma_\alpha^4} \left(\mathbf{J}_r(\beta_{12} + \frac{\pi}{2}) + \mathbf{J}_r(\beta_{21} + \frac{\pi}{2}) \right), \quad (53)$$

where the latter step uses the definition of the RDM in (21), and the fact that $r_{12} = r_{21} = r$. As $\mathbf{J}_r(\beta_{12} + \frac{\pi}{2}) = \mathbf{J}_r(\beta_{21} + \frac{\pi}{2})$, we can further condense this to

$$\mathbf{E} = \frac{2}{r^2 \sigma_\alpha^4} \left(\mathbf{J}_r(\beta' + \frac{\pi}{2}) \right) \quad (54)$$

where $\beta' = \beta_{12}$ or $\beta' = \beta_{21}$. For ease of notation, we then finally introduce $\mathbf{H} = \mathbf{S}_{12} + \mathbf{S}_{21} - \gamma \mathbf{E}$, and write $\mathbf{J}_e(\mathbf{p})$ as in (22).

APPENDIX C PROOF OF PROPOSITION 3

Starting from (22), we can express

$$\mathbf{J}_e(\mathbf{p}_1) \quad (55)$$

$$= [\mathbf{J}_e(\mathbf{p})]_{1:2,1:2} - [\mathbf{J}_e(\mathbf{p})]_{1:2,3:4} [\mathbf{J}_e(\mathbf{p})]_{3:4,3:4}^{-1} [\mathbf{J}_e(\mathbf{p})]_{3:4,3:4} \quad (56)$$

$$= \Sigma_{11}^{-1} + \mathbf{H} - \mathbf{H} (\Sigma_{22}^{-1} + \mathbf{H})^{-1} \mathbf{H}. \quad (57)$$

The matrix \mathbf{H} can be decomposed as $\mathbf{H} = \sum_{n=1}^2 \lambda_n^{\mathbf{H}} \mathbf{u}_n \mathbf{u}_n^T$, where $\lambda_n^{\mathbf{H}}$ and \mathbf{u}_n are eigenvalues and eigenvectors, respectively. Given that $\Sigma_{22} = \sigma_{G,2}^2 \mathbf{I}_2$ it is straightforward to show that the matrix $(\Sigma_{22}^{-1} + \mathbf{H})^{-1}$ has the same eigenvectors as the matrix \mathbf{H} , so that $(\Sigma_{22}^{-1} + \mathbf{H})^{-1} = \sum_{n=1}^2 \lambda_n^{\mathbf{U}} \mathbf{u}_n \mathbf{u}_n^T$ with eigenvalues $\lambda_n^{\mathbf{U}} = 1/(\lambda_n^{\mathbf{H}} + 1/\sigma_{G,2}^2)$. Based on this we can then write the EFIM for position \mathbf{p}_1 as

$$\begin{aligned} \mathbf{J}_e(\mathbf{p}_1) &= \Sigma_{11}^{-1} + \sum_{n=1}^2 \lambda_n^{\mathbf{H}} \mathbf{u}_n \mathbf{u}_n^T \\ &\quad - \sum_{n=1}^2 \lambda_n^{\mathbf{H}} \mathbf{u}_n \mathbf{u}_n^T \sum_{n=1}^2 \lambda_n^{\mathbf{U}} \mathbf{u}_n \mathbf{u}_n^T \sum_{n=1}^2 \lambda_n^{\mathbf{H}} \mathbf{u}_n \mathbf{u}_n^T \end{aligned} \quad (58)$$

$$\stackrel{(a)}{=} \Sigma_{11}^{-1} + \sum_{n=1}^2 \lambda_n^{\mathbf{H}} \mathbf{u}_n \mathbf{u}_n^T - \sum_{n=1}^2 (\lambda_n^{\mathbf{H}})^2 \lambda_n^{\mathbf{U}} \mathbf{u}_n \mathbf{u}_n^T \quad (59)$$

$$= \Sigma_{11}^{-1} + \sum_{n=1}^2 \lambda_n^{\mathbf{H}} (1 - \lambda_n^{\mathbf{H}} \lambda_n^{\mathbf{U}}) \mathbf{u}_n \mathbf{u}_n^T. \quad (60)$$

where (a) uses that the different eigenvectors are orthogonal (i.e., $\mathbf{u}_n^T \mathbf{u}_m^T = 0$ for $n \neq m$). Then, inserting the expression for $\lambda_n^{\mathbf{U}}$ from above, and using that $\Sigma_{11} = \sigma_{G,1}^2 \mathbf{I}_2$ we obtain

$$\mathbf{J}_e(\mathbf{p}_1) = \frac{1}{\sigma_{G,1}^2} \mathbf{I}_2 + \sum_{n=1}^2 \kappa_n \lambda_n^{\mathbf{H}} \mathbf{u}_n \mathbf{u}_n^T \quad (61)$$

where $\kappa_n = (1 - \lambda_n^{\mathbf{H}}/(\lambda_n^{\mathbf{H}} + 1/\sigma_{G,2}^2))$.

What remains now is to analyze the eigenvalues and eigenvectors of the matrix $\mathbf{H} = \mathbf{S}_{12} + \mathbf{S}_{21} - \gamma \mathbf{E}$. Using the expression for the radar covariance in (5), we can write

$$\mathbf{S}_{ij} = \mathbf{R}^T(\psi_i) \left(\mathbf{R}^T(\alpha_{ij}) \underbrace{\begin{bmatrix} \sigma_r^2 & 0 \\ 0 & (r_{ij} \sigma_\alpha)^2 \end{bmatrix}}_{\Sigma_{ij}^{P^*}} \mathbf{R}(\alpha_i) \right) \mathbf{R}(\psi_{ij}). \quad (62)$$

As the inner matrix $\Sigma_{ij}^{P^*}$ has eigenvalues σ_r^2 and $(r_{ij} \sigma_\alpha)^2$ with corresponding eigenvectors $[1; 0]$ and $[0; 1]$ it is then straight forward to show that the matrix \mathbf{S}_{ij} has eigenvalues $\lambda_1^{\mathbf{S}_{ij}} = 1/\sigma_r^2$ and $\lambda_2^{\mathbf{S}_{ij}} = \frac{1}{(r_{ij} \sigma_\alpha)^2}$, with corresponding eigenvectors $\mathbf{u}_1^{\mathbf{S}_{ij}} = [\cos(\beta_{ij}); \sin(\beta_{ij})]$ and $\mathbf{u}_2^{\mathbf{S}_{ij}} = [\cos(\beta_{ij} + \frac{\pi}{2}); \sin(\beta_{ij} + \frac{\pi}{2})]$ in which $\beta_{ij} = \psi_i + \alpha_{ij}$. Using this in combination with (23) and the fact that $\mathbf{u}_n^{\mathbf{S}_{12}} (\mathbf{u}_n^{\mathbf{S}_{12}})^T = \mathbf{u}_n^{\mathbf{S}_{21}} (\mathbf{u}_n^{\mathbf{S}_{21}})^T$ we can then express \mathbf{H} as

$$\mathbf{H} = \sum_{n=1}^2 \lambda_n^{\mathbf{S}_{12}} \mathbf{u}_n \mathbf{u}_n^T + \sum_{n=1}^2 \lambda_n^{\mathbf{S}_{21}} \mathbf{u}_n \mathbf{u}_n^T - \frac{2\gamma}{r^2 \sigma_\alpha^4} \mathbf{u}_2 \mathbf{u}_2^T \quad (63)$$

where $\mathbf{u}_1 = [\cos(\beta'); \sin(\beta')]$, $\mathbf{u}_2 = [\cos(\beta' + \pi/2); \sin(\beta' + \pi/2)]$, and β' is either β_{12} or β_{21} . Inserting the eigenvalues for the matrices \mathbf{S}_{12} and \mathbf{S}_{21} , and using that $r_{12} = r_{21} = r$ we then obtain

$$\mathbf{H} = \underbrace{\frac{2}{\sigma_r^2}}_{\lambda_1^{\mathbf{H}}} \mathbf{u}_1 \mathbf{u}_1^T + \underbrace{\frac{2}{r^2} \left(\frac{1}{\sigma_\alpha^2} - \frac{\gamma}{\sigma_\alpha^4} \right)}_{\lambda_2^{\mathbf{H}}} \mathbf{u}_2 \mathbf{u}_2^T. \quad (64)$$

Plugging this back in to (61) and writing it in terms of RDMs leads to (24)

REFERENCES

- [1] P. Koopman and M. Wagner, "Autonomous Vehicle Safety: An Interdisciplinary Challenge," *IEEE Intelligent Transportation Systems Magazine*, vol. 9, no. 1, pp. 90–96, Spring 2017.
- [2] J. Ziegler, P. Bender, M. Schreiber, H. Lategahn, T. Strauss, C. Stiller et al., "Making Bertha Drive - An Autonomous Journey on a Historic Route," *IEEE Intelligent Transportation Systems Magazine*, vol. 6, no. 2, pp. 8–20, 2014.
- [3] L. A. Klein, *ITS Sensors and Architectures for Traffic Management and Connected Vehicles*. CRC Press, 2017.
- [4] M. Gerla, E. Lee, G. Pau, and U. Lee, "Internet of vehicles: From intelligent grid to autonomous cars and vehicular clouds," in *2014 IEEE World Forum on Internet of Things (WF-IoT)*, March 2014, pp. 241–246.
- [5] L. Kong, M. K. Khan, F. Wu, G. Chen, and P. Zeng, "Millimeter-Wave Wireless Communications for IoT-Cloud Supported Autonomous Vehicles: Overview, Design, and Challenges," *IEEE Communications Magazine*, vol. 55, no. 1, pp. 62–68, January 2017.
- [6] K. Sjöberg, P. Andres, T. Buburuzan, and A. Brakemeier, "Cooperative Intelligent Transport Systems in Europe: Current Deployment Status and Outlook," *IEEE Vehicular Technology Magazine*, vol. 12, no. 2, pp. 89–97, June 2017.
- [7] R. Hult, G. R. Campos, E. Steinmetz, L. Hammarstrand, P. Falcone, and H. Wymeersch, "Coordination of Cooperative Autonomous Vehicles: Toward safer and more efficient road transportation," *IEEE Signal Processing Magazine*, vol. 33, no. 6, pp. 74–84, Nov 2016.
- [8] L. Chen and C. Englund, "Cooperative Intersection Management: A Survey," *IEEE Transactions on Intelligent Transportation Systems*, vol. 17, no. 2, pp. 570–586, Feb.
- [9] H. Li and F. Nashashibi, "Cooperative Multi-Vehicle Localization Using Split Covariance Intersection Filter," *IEEE Intelligent Transportation Systems Magazine*, vol. 5, no. 2, pp. 33–44, Summer 2013.
- [10] F. d. P. Müller, "Survey on Ranging Sensors and Cooperative Techniques for Relative Positioning of Vehicles," *Sensors*, vol. 7, no. 2, 2017.
- [11] F. d. P. Müller, E. M. Diaz, and I. Rashdan, "Cooperative positioning and radar sensor fusion for relative localization of vehicles," in *IEEE Intelligent Vehicles Symposium (IV)*, June 2016, pp. 1060–1065.
- [12] M. Rockl, "Cooperative Situation Awareness in Transportation," Ph.D. dissertation, University of Innsbruck, 2009.
- [13] M. Obst, L. Hobert, and P. Reisdorf, "Multi-sensor data fusion for checking plausibility of V2V communications by vision-based multiple-object tracking," in *2014 IEEE Vehicular Networking Conference (VNC)*, Dec 2014, pp. 143–150.

- [14] S. Kim, B. Qin, Z. J. Chong, X. Shen, W. Liu, M. H. Ang, E. Frazzoli, and D. Rus, "Multivehicle Cooperative Driving Using Cooperative Perception: Design and Experimental Validation," *IEEE Transactions on Intelligent Transportation Systems*, vol. 16, no. 2, pp. 663–680, April 2015.
- [15] "Automotive vertical sector," 5G-PPP, White Paper, 2015.
- [16] Deliverable D2.1, "5GCAR Scenarios, Use Cases, Requirements and KPIs," 5G-PPP, Tech. Rep., Aug 2017.
- [17] HIGHTS project deliverable D2.1, "Use cases and Application Requirements," Tech. Rep., Mar 2016.
- [18] European Automobile Manufacturers Association (ACEA), "ACEA Report: Vehicles in use Europe 2017," 2017. [Online]. Available: https://www.acea.be/uploads/statistic_documents/ACEA_Report_Vehicles_in_use-Europe_2017.pdf
- [19] X. Mosquet, T. Dauner, N. lang, M. Russman, A. Mei-Pochtler, R. Agrawal, and F. Schmiege, "Revolution in the Drivers's Seat: The Road to Autonomous Vehicles," Boston Consulting Group, Tech. Rep., Apr. 2015. [Online]. Available: http://image-src.bcg.com/Images/BCG-Revolution-in-the-Drivers-Seat-Apr-2015_tcm9-64351.pdf
- [20] "Market forecast for connected and autonomous vehicles," Catapult Transport Systems, Tech. Rep., Jul. 2017. [Online]. Available: https://www.gov.uk/government/uploads/system/uploads/attachment_data/file/642813/15780_TSC_Market_Forecast_for_CAV_Report_FINAL.pdf
- [21] "ITS-G5 technology - A Fact Sheet." [Online]. Available: <https://itsg5-ready-to-roll.eu/ITS-G5-FactSheet.pdf>
- [22] "Share of New Cars Sold That Are Connected to The Internet Worldwide from 2015 to 2025," Accenture, Tech. Rep., 2015, Statista - The Statistics Portal. [Online]. Available: www.statista.com/statistics/275849/number-of-vehicles-connected-to-the-internet/
- [23] D. Wang, K. O'Keefe, and M. Petovello, "Decentralized Cooperative Positioning for Vehicle-to-Vehicle (V2V) Application Using GPS Integrated with UWB Range," in *Proceedings of the ION 2013 Pacific PNT Meeting.*, Apr. 2013, pp. 793–803.
- [24] J. Wang, Y. Gao, Z. Li, X. Meng, and C. M. Hancock, "A Tightly-Coupled GPS/INS/UWB Cooperative Positioning Sensors System Supported by V2I Communication," vol. 16, no. 7, Jun. 2016.
- [25] S. Al-Stouhi and R. Miucic, "Absolute Localization via DSRC Signal Strength," in *2016 IEEE 84th Vehicular Technology Conference (VTC-Fall)*, Sep. 2016, pp. 1–5.
- [26] F. Shen, J. W. Cheong, and A. G. Dempster, "A DSRC Doppler/IMU/GNSS Tightly-coupled Cooperative Positioning Method for Relative Positioning in VANETs," *Journal of Navigation*, vol. 70, no. 1, p. 120?136, 2017.
- [27] A. Shahmansoori, G. E. Garcia, G. Destino, G. Seco-Granados, and H. Wymeersch, "Position and Orientation Estimation Through Millimeter-Wave MIMO in 5G Systems," *IEEE Transactions on Wireless Communications*, vol. 17, no. 3, pp. 1822–1835, March 2018.
- [28] Y. Shen, H. Wymeersch, and M. Z. Win, "Fundamental Limits of Wide-band Localization; Part II: Cooperative Networks," *IEEE Transactions on Information Theory*, vol. 56, no. 10, pp. 4981–5000, Oct 2010.
- [29] R. M. Buehrer, H. Wymeersch, and R. M. Vaghefi, "Collaborative Sensor Network Localization: Algorithms and Practical Issues," *Proceedings of the IEEE*, vol. 106, no. 6, pp. 1089–1114, June 2018.
- [30] H. Wymeersch, G. Seco-Granados, G. Destino, D. Dardari, and F. Tufvesson, "5G mmWave Positioning for Vehicular Networks," *IEEE Wireless Communications*, vol. 24, no. 6, pp. 80–86, Dec 2017.
- [31] J. Gabela, S. Goel, A. Kealy, and M. Hedley, "Cramér Rao Bound Analysis for Cooperative Positioning in Intelligent Transportation Systems," in *IGNSS Symposium 2018*, Feb. 2018.
- [32] Y. Wang, G. de Veciana, T. Shimizu, and H. Lu, "Performance and Scaling of Collaborative Sensing and Networking for Automated Driving Applications," in *2018 IEEE International Conference on Communications Workshops (ICC Workshops)*, vol. 16, no. 7, May 2018.
- [33] K. Granström, M. Baus, and S. Reuter, "Extended Object Tracking: Introduction, Overview, and Applications," *Journal of Advances in Information Fusion*, vol. 12, no. 2, Dec. 2017.
- [34] D. Kong and X. Guo, "Analysis of vehicle headway distribution on multi-lane freeway considering car-truck interaction," *Advances in Mechanical Engineering*, vol. 8, no. 4, 2016.
- [35] I. Greenberg, *The Log Normal Distribution of Headway Times*, ser. Report (Port of New York Authority. Tunnels and Bridges Department Research Division). Port of New York Authority, 1964. [Online]. Available: https://books.google.se/books?id=_QOpHAAACAAJ
- [36] S. Yin, Z. Li, Y. Zhang, D. Yao, Y. Su, and L. Li, "Headway distribution modeling with regard to traffic status," in *2009 IEEE Intelligent Vehicles Symposium*, June 2009, pp. 1057–1062.
- [37] Oxford Technical Solutions, "RT3000V2 GNSS INS for high dynamic vehicle testing," Datasheet.
- [38] Bosch, "Chassis Systems Control Mid-range radar sensor (MRR) for front and rear applications," Datasheet.



Erik Steinmetz received his M.Sc. degree in Electrical Engineering from Chalmers University of Technology, Sweden, in 2009. He is currently a research and development engineer with RISE Research Institutes of Sweden. He is also affiliated with the Department of Electrical Engineering at Chalmers University of Technology, where he is working towards his Ph.D. degree. His research interests include positioning, sensor fusion, communication and controls applied within the fields of intelligent vehicles and cooperative automated driving.



Ragne Emardson received his M.Sc in Computer Science and Engineering and Ph.D in Electrical Engineering from Chalmers University of Technology in 1992 and 1998 respectively. From 1998 to 2000, he was a postdoctoral researcher with the Jet Propulsion Laboratory, California Institute of Technology. He has also held positions with Ericsson Mobile Data Design, Saab Ericsson Space and RISE Research Institutes of Sweden. Currently, he is dean of faculty at University of Borås. His research interests include Global Navigation Satellite Systems, mathematical modeling, and measurement uncertainty evaluation.



Fredrik Brännström received the M.Sc. degree from Luleå University of Technology, Luleå, Sweden, in 1998, and the Ph.D. degree in Communication Theory from the Department of Computer Engineering, Chalmers University of Technology, Gothenburg, Sweden, in 2004. From 2004 to 2006, he was a Post-Doctoral Researcher at the Department of Signals and Systems, Chalmers University of Technology. From 2006 to 2010, he was a Principal Design Engineer with Quantenna Communications, Inc., Fremont, CA, USA. He is currently Professor and Head of Communication Systems Group, Department of Electrical Engineering, Chalmers University of Technology, Gothenburg, Sweden. His current research interests include algorithms, resource allocation, synchronization, antenna concepts, and protocol design for vehicular communication systems, as well as different applications of coding.



Henk Wymeersch (S'99, M'05) is a Professor with the Department of Electrical Engineering at Chalmers University of Technology, Sweden. Prior to joining Chalmers, he was a postdoctoral researcher from 2005 until 2009 with the Laboratory for Information and Decision Systems at the Massachusetts Institute of Technology. Henk Wymeersch obtained the Ph.D. degree in Electrical Engineering/Applied sciences in 2005 from Ghent University, Belgium. He served as Associate Editor for *IEEE Communication Letters* (2009-2013), *IEEE Transactions on Wireless Communications* (since 2013), and *IEEE Transactions on Communications* (since 2016). He is the author or Iterative Receiver Design (Cambridge University Press, 2007). His current research interests include cooperative systems and intelligent transportation.